NUMERICAL SIMULATION OF THE TRANSONIC BLADE-VORTEX INTERACTION

Nguk-Lan Ng & Richard Hillier
Imperial College of Science, Technology & Medicine
London SW7, UK

Abstract

The transonic, parallel blade-vortex interaction (BVI) has been investigated numerically. Simulations of the unsteady interaction are made using a time accurate, high resolution Euler code based on a second-order Godunov-type method. The incident vortex has an assumed structure based on Sculley's velocity profile.

A local mesh refinement scheme along the lines of that developed by Berger (Ref 1,2,3), is described. The method is based on embedded meshes and allows the resolution of flow/geometric features to be increased without prohibitive expense. The behaviour of the mesh interfaces for this scheme are also examined.

Numerical test cases are presented which demonstrate the ability of the code to simulate steady and unsteady flows about a NACA0012 aerofoil.

The nature of the interaction for a free stream Mach number of $M_\infty = 0.8$, is considered in detail. The flow for this case is transonic and three sources of noise generation have been identified. These involve flow mechanisms at the leading edge, at the trailing edge and at the shocks. The nature of the noise generation is found to be highly directional.

For small vortex-blade offsets, the blade interacts with the 'near-field' of the vortex, where the associated induced velocities and flow gradients result in a highly impulsive interaction. For close interactions the dependence of the interaction on the assumed vortex structure is evident. This dependence is examined by considering the effect of core size on the flow. As the vortex-blade offset is increased, and the interaction becomes less intense, the change in the nature of the noise generation is also examined.

Nomenclature

a = local acoustic speed
a_∞ = ambient acoustic speed
A = normalised circulation, Γ/Γ_t
c = chord length
C_L = lift coefficient, $L/\frac{1}{2}\rho U_\infty^2 c$
C_P = pressure coefficient, $(p - p_\infty)/\frac{1}{2}\rho U_\infty^2$
Γ_t = total circulation of the vortex
Γ_c = circulation at the core radius
$\hat{\Gamma}$ = normalised circulation, $\Gamma/U_\infty c$
M_∞ = Free stream Mach number
p = fluid pressure
p_∞ = ambient fluid pressure
r = radial distance from the vortex centre
r_c = core radius
$\tilde{r}$ = normalised radial distance, r/r_c
ρ = fluid density
ρ_∞ = ambient fluid density
t = time
$\tilde{t}$ = normalised time, $U_\infty t/c$
U_θ = circumferential velocity
U_∞ = free stream velocity
$\bar{v}$ = velocity vector

Introduction

The interaction of convected disturbances with blades is a commonly occuring phenomenon in modern day machinery within aeronautics. In particular the problem of blade-vortex interactions (BVI) has been of interest to researchers for many years, notably within the field of rotorcraft flow analysis, where blades must operate in close proximity to their own wake. In certain circumstances, such as during powered descent or during particular airborne manoeuvres, trailing tip vortices can be ingested into the rotor disk, resulting in varying degrees of interaction. Another example of rotorcraft BVI occurs when trailing vortices shed by the main rotor blades are convected towards the tail rotors.

BVI is seen as being predominantly responsible for the sudden changes in blade loading, resulting in both impulsive noise generation *and* possible problems with fatigue failure. Most of the research into BVI has been motivated by the acoustic aspects of the interaction as the generated noise is generally considered to be the most annoying type – impulsive, directional, and in the middle of the audible frequency range. Sound generation due to BVI is also seen as a significant problem because it usually occurs when the rotorcraft is landing. The nature of the operational use of rotorcraft is such that this is often in densely populated areas, where noise pollution is highly objectionable. The historical interest in BVI noise is detailed by Leverton (Ref 4).

The flow field around rotorcraft is highly three dimensional and extremely complex, and a comprehensive theory which encompasses the many flow interactions about the rotorcraft remains elusive. Many of the helicopters in use today have high aspect ratio rotor blades where the tip Mach numbers can be transonic. The presence of shock waves in the flow field further complicates issues, making the understanding of the relevant flow mechanisms more difficult. For this reason all the analytical and numerical work, up to this day, that has looked at the BVI problem has incorporated simplifying assumptions, such as two dimensionality, incompressibility

or inviscid flow. For example, Obermeier & Zhu (Ref 5) examine the low speed ($M_\infty = 0.4$) interaction making incompressible approximations to the governing equations. Jones & Caradonna (Ref 6) and Caradonna & Strawn (Ref 7), however, consider higher Mach number cases up to the transonic interaction, using potential methods. The assumption of inviscid flow has been made by Srinivasan *et al.* (Ref 8) and Srinivasan & McCroskey (Ref 9), in which the prescribed vortex method is also used. The premise of this method is that more accurate solutions can be obtained by imposing the vortex on to the flow field, and assuming that the vortex structure is unaffected by the interaction. Although this counteracts problems due to the numerical diffusion of the vortex, it does not allow for distortion of the core, which Caradonna and Strawn suggest may be important.

Experimental studies have also been restricted by the complexity of the flow field, generally considering the interaction in the absence of the helicopter body and tail rotor, with much work, such as that by Booth (Ref 10), Kalkhoran & Wilson (Ref 11), Lent *et al.* (Ref 12) and Lee & Bershader (Ref 13) focussing on the quasi-two dimensional problem.

The present paper is directed towards the unsteady numerical simulation of the inviscid, transonic BVI, using a time accurate, high resolution Euler code based on a second-order Godunov-type method. The aims of this simulation are twofold, (i) to investigate the near-field flow physics, and (ii) to provide data for far-field acoustic predictions.

We intend to progress towards our eventual aim of the simulation of the three-dimensional case, by examining first the purely two-dimensional interaction. This paper, therefore, is concerned with two-dimensional interaction. Consideration of this case is useful as both a code validation exercise, and also as an approximation to one of the limiting cases of the generic three-dimensional problem - parallel BVI.

Governing equations

For the results presented in this paper the flow is assumed to be two-dimensional, compressible, inviscid and non-heat conducting. Therefore, computations involve the numerical solution of the two-dimensional Euler equations,

$$\frac{\partial U}{\partial t} + \frac{\partial F}{\partial x} + \frac{\partial G}{\partial y} = 0 \qquad (1)$$

where,

$$U = \begin{bmatrix} \rho \\ \rho u \\ \rho v \\ E \end{bmatrix} \qquad (2)$$

and F and G are arrays of the flux terms,

$$F = \begin{bmatrix} \rho u \\ \rho u^2 + p \\ \rho uv \\ u(E+p) \end{bmatrix}, G = \begin{bmatrix} \rho v \\ \rho uv \\ \rho v^2 + p \\ v(E+p) \end{bmatrix} \qquad (3)$$

In the above equations E is the total energy, and the relationship between E and p is given by the equation of state for a polytropic gas,

$$p = (\gamma - 1)\left[E - \frac{1}{2}\rho(u^2 + v^2)\right] \qquad (4)$$

Computational Method

The Euler equations are solved using an explicit, second-order upwind Godunov-type solver, extended by Hillier from the work of Ben-Artzi & Falcowitz (Ref 14). Hillier (Ref 15) has demonstrated the solver's ability to produce the high resolution capture of pressure and vortical features. Flow values are held at cell centres and piecewise-linear spatial gradients are reconstructed using a monotone constraint. Having determined the flow gradients in this manner, the fluxes at cell interfaces are calculated to second order accuracy by assuming a generalised Riemann problem (GRP). For the solution of two-dimensional problems an operator-split method is used. The solution is explicitly time-marched from a prescribed initialised state in a time accurate manner.

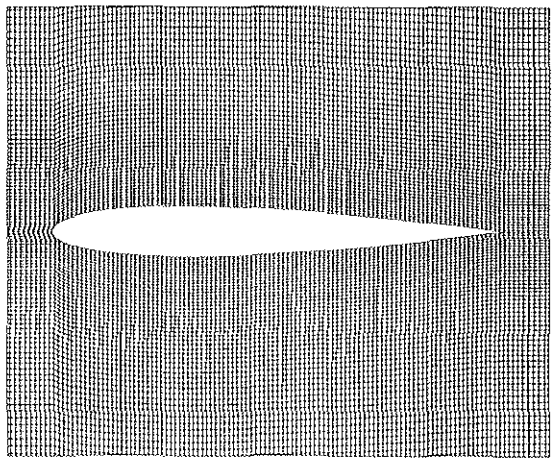

Figure 1: Mesh about a NACA0012 aerofoil

The computational domain is discretised using a structured mesh as shown in figure 1. The mesh is body-fitted and curvilinear close to the aerofoil, asymptoting to Cartesian in the far-field. This Cartesian geometry is seen as advantageous as it does not suffer from an intrinsic fall-off in resolution in the far-field, as would happen with a C-grid, for example. The advantages of this are twofold. Firstly the mesh is suited to the convection of the incident vortex from upstream, and secondly there

are no major resolution penalties for simulating the flow with different vortex-blade offsets.

Local Mesh Refinement

The results presented in this paper have been computed using structured meshes similar to the one shown in figure 1. However, there are two particular problems associated with this technique. Firstly increasing refinement in areas of interest in the flow also results in an increase in cell density where it is not necessarily required. Secondly, the time marching of the solution is restricted by the stable time step of the smallest cell in the domain. In response to these problems a local mesh refinement technique has been developed, based on the adaptive mesh refinement (AMR) scheme established by Berger (Ref 1,2,3) and developed by Quirk (Ref 16).

Refinement of the mesh is made by 'embedding' additional meshes in the regions of the flow where increased geometric/flow resolution is required (see figure 3). The main characteristics of these embedded meshes are,

- There is a hierarchical system of meshes, the coarsest of which defines the extent of the computational domain. See figure 2
- Meshes at different levels of resolution can coexist in the same regions of the computational domain ie. finer meshes overlay coarser ones. See figure 3
- Finer meshes are generated by the subdivision of cells of coarser meshes. Therefore, the boundaries of the finer meshes coincide with the cell walls of underlying mesh.

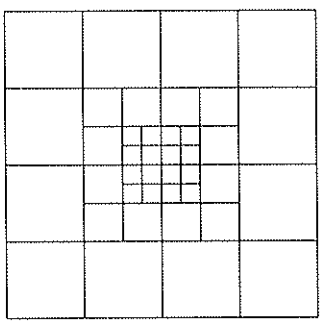

Figure 2: Local mesh refinement – generation of fine meshes by cell subdivision

The overall grid, therefore, is composed of the base mesh and a number of overlaid refined meshes. All of the meshes are structured and at each time step their associated flow fields are solved independently. The actual flow solver is 'unaware' of relationship between meshes. It should be emphasised then that the meshes are to a large degree autonomous, possessing their own mesh data and flow solution. Communication between meshes takes place at interfaces prior to integration and when fine solutions are projected down on to coarse meshes after integration.

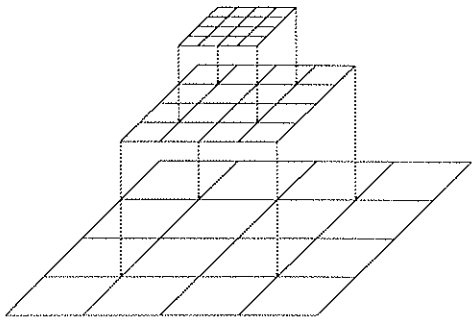

Figure 3: Local mesh refinement – embedding of fine meshes

Figure 4 shows a grid which has been designed for the simulation of a vortex passing beneath a NACA0012 aerofoil. Meshes have been embedded to increase the geometric resolution of the blade, and flow resolution of the near field and the convecting vortex. Note that at the moment, although the mesh can be refined, the mesh is *not* adaptive.

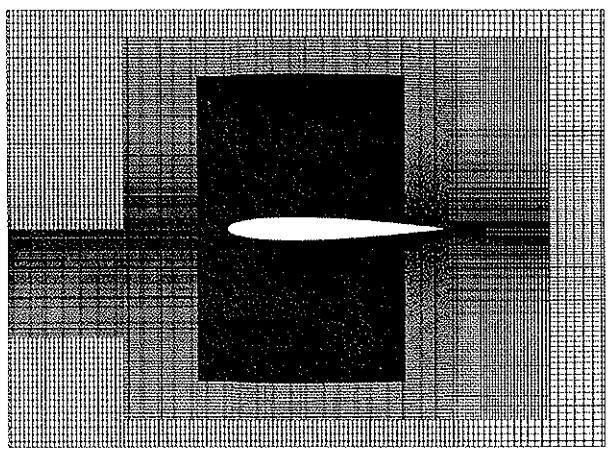

Figure 4: Local mesh refinement – grid for 2D BVI

As well as local mesh refinement, another key feature of this scheme is the time marching of the solution. Cells are no longer all updated by the same time step. Instead meshes are updated by time steps which vary depending on their level of refinement ie. the higher their level of refinement, the smaller the time step. In order to maintain time accuracy, therefore, it is important to carefully coordinate the updating of each of the meshes.

Despite the increased complexity of this coordination process, temporal refinement has the advantage that the updating of coarse meshes is not unduly restricted by the stable time step of the smallest cells

of the grid. This is the main reason for the increased efficiency of the code.

Boundary Conditions

The numerical simulation of any flow mechanism inevitably involves a compromise between the desire to model the physical flow as closely as possible, and the limitations imposed by computer resources. A general consequence of this compromise is the restriction of the simulation to a finite region of the physical flow field. This inexorably leads to errors in the solution, and the role of the far field boundary conditions becomes crucial in minimising these errors. It is important, therefore, that the boundary conditions are carefully considered and provide a good approximation of the effect of the far field on the numerical domain.

At the far field boundaries the boundary conditions proposed by Giles (Ref 17) have been implemented.

The analysis by Giles considers boundary conditions for the one dimensional characteristics, which are defined below,

$$\begin{bmatrix} c_1 \\ c_2 \\ c_3 \\ c_4 \end{bmatrix} = \begin{bmatrix} -a^2 & 0 & 0 & 1 \\ 0 & 0 & \rho a & 0 \\ 0 & \rho a & 0 & 1 \\ 0 & -\rho a & 0 & 1 \end{bmatrix} \begin{bmatrix} \delta\rho \\ \delta v_n \\ \delta v_t \\ \delta p \end{bmatrix} \quad (5)$$

where $\delta\rho$, δv_n, δv_t, δp represent perturbations from uniform conditions . It can be seen from this definition that c_1 represents an entropy wave, c_2 a vorticity wave and c_3 and c_4 the right and left acoustic waves respectively.

Analysis carried out by Giles results in the following approximate, two dimensional boundary conditions,

Inflow boundary conditions

$$\frac{\partial}{\partial t}\begin{bmatrix} c_1 \\ c_2 \\ c_3 \end{bmatrix} + A\frac{\partial}{\partial x_t}\begin{bmatrix} c_1 \\ c_2 \\ c_3 \\ c_4 \end{bmatrix} = 0 \quad (6)$$

where,

$$A = \begin{bmatrix} v_t & 0 & 0 & 0 \\ 0 & v_t & (a+v_n)/2 & (a-v_n)/2 \\ 0 & (a-v_n)/2 & v_t & 0 \end{bmatrix}$$

These boundary conditions provide conditions for the three incoming characteristics. The outgoing characteristic, c_4 is extrapolated from interior values which is consistent with the physical one dimensional problem.

Outflow boundary conditions

$$\frac{\partial c_4}{\partial t} + \begin{bmatrix} 0 & v_n & 0 & v_t \end{bmatrix}\frac{\partial}{\partial x_t}\begin{bmatrix} c_1 \\ c_2 \\ c_3 \\ c_4 \end{bmatrix} = 0 \quad (7)$$

These boundary conditions are found to be second order accurate and provide values for the one incoming characteristic, c_4. The other three outgoing characteristic variables are extrapolated from the interior.

Vortex Model

In the physical blade-vortex interaction the vortex is generated upstream of the aerofoil at a preceding blade. However, given the limitation of computational resources, simulation of this vortex forming process is impractical and so a vortex must be instantaneously initialised in the flow field upstream of the blade, at the start of the computation. This imposition of an assumed vortical flow field naturally raises the issue of how this vortex should be modelled, and how important the vortex structure is to the computation.

Experimental results from Tung *et al.* (Ref 18) suggest that under typical operating conditions the strength of the trailing tip vortex equals the maximum bound circulation, irrespective of the blade configuration. The vortex is also found to be turbulent, and following work by Hoffman & Joubert (Ref 19) a model for the turbulent vortex is proposed that divides the vortex in to four distinct flow regions.

1. *Viscous core.* This is the laminar innermost region where viscous diffusion is dominant and the rotation is solid body type ie. rotational flow with the circulation increasing as the square of the distance from the centre.

2. *Turbulent mixing region.* Flow within this region is dominated by turbulent diffusion and the tangential velocity reaches a maximum.

3. *Transition region.* This is where the turbulent region makes a transition to the outer, inviscid region. It is an extremely variable part of the vortex and the transition is not a smooth one, especially for vortices in the early stages of development. Transition appears to happen in discrete jumps due to the effect of the vorticity sheet spiralling into the vortex.

4. *Irrotational region.* This is the outermost region of the vortex where circulation is constant.

Based on their experimental data Tung *et al.* derive empirical expressions for the variation of circulation with distance from the vortex centre. This circulation profile is shown in figure 5.

Lee & Bershader (Ref 13) derive similar expressions, based on experimental measurements of a quasi-two dimensional starting vortex generated in a shock tube. These are given below and are also shown in figure 5.

Region 1: $A = 0.80 r_c^2$ $\quad 0 \leq r_c \leq 0.62$
Region 2: $A = 0.51 + 0.43 \ln(r_c)$ $\quad 0.62 < r_c \leq 1.8$
Region 3: $A = 1 - 0.8 \exp[-0.65 r_c]$ $\quad 1.8 < r_c$

Srinivasan *et al.* (Ref 8) and Caradonna & Strawn (Ref 7) show that the effectiveness of any numerical simulation of BVI is strongly dependent on the assumed vortex structure, since the miss distances of interest are of order of the core radius. A commonly used algebraic model is Sculley's (Ref 8) velocity profile,

$$U_\theta = \frac{\Gamma}{2\pi} \frac{r}{r^2 + a^2} \tag{8}$$

which gives a distribution for the tangential velocity, U_θ.

Another common model for the tangential velocity profile, is the Rankine vortex, which has a solidly rotating core and zero vorticity away from the core. The circulation profiles of both of these models is shown in figure 5. It is apparent from this figure that there is a good agreement between Sculley's model and the experimental results of Lee & Bershader. Since we are concerned primarily with the two dimensional case, the empirical profile of Lee & Bershader is seen as the more relevant case.

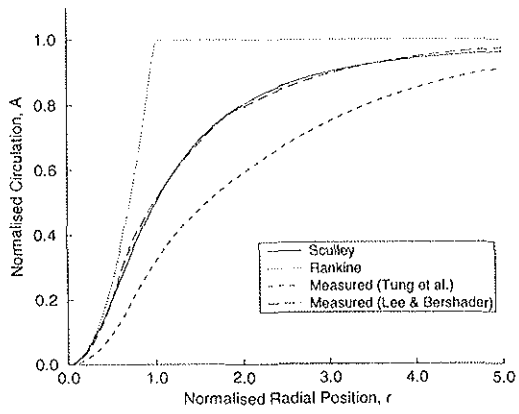

Figure 5: Circulation profiles of vortex models compared to experimental data

For all the computations presented in this paper the initialised vortex structure is defined by Sculley's velocity profile together with, the radial momentum equation,

$$\frac{dp}{dr} = \frac{\rho U_\theta^2}{r} \tag{9}$$

and assumptions of a constant temperature core,

$$p = \rho R T \quad , \quad \tilde{r} \leq 1 \tag{10}$$

and constant entropy elsewhere,

$$p = k_1 \rho^\gamma \quad , \quad \tilde{r} \geq 1 \tag{11}$$

Numerical Test Cases

The following test cases have been used to examine the ability of the current code to simulate flows about a NACA0012 aerofoil. The effect of using embedded meshes is also examined. Of particular interest is the behaviour of the solution at mesh interfaces, where there is a discontinuity in mesh resolution.

Steady test case

The first case is an AGARD Fluid Dynamics Panel test case [1] (Test Case 01) for the steady flow around a NACA0012 aerofoil at a Mach number $M_\infty = 0.8$, and angle of incidence, $\alpha = 1.25^o$.

This flow has been computed using a the single structured mesh shown in figure 1 as well as the locally refined version of this mesh.

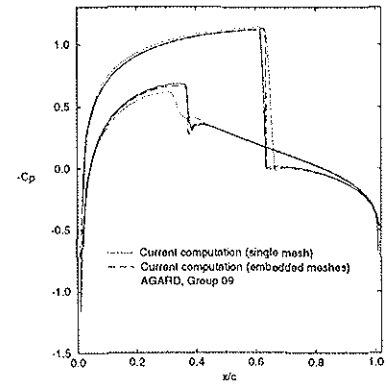

(a)

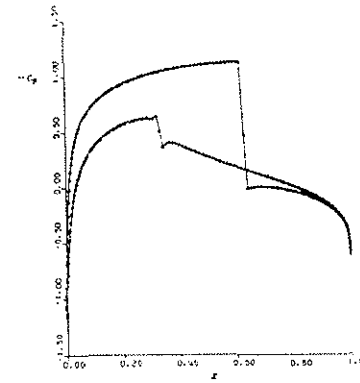

(b)

Figure 6: Surface pressure distributions for AGARD Panel Test Case 01

[1] *AGARD Advis. Rep. No.211* (1985)

Figure 6 shows calculated distributions of the pressure coefficient along the upper and lower surfaces of the aerofoil, for the above test case. Results from the current computation (both for a single and embedded meshes) are compared with solutions from group 9 (Schmidt W & Jameson A) of the AGARD Panel, in figure 6(a) and with the improved shock capturing scheme of Van der Berg *et al.* (Ref 20) in figure 6(b).

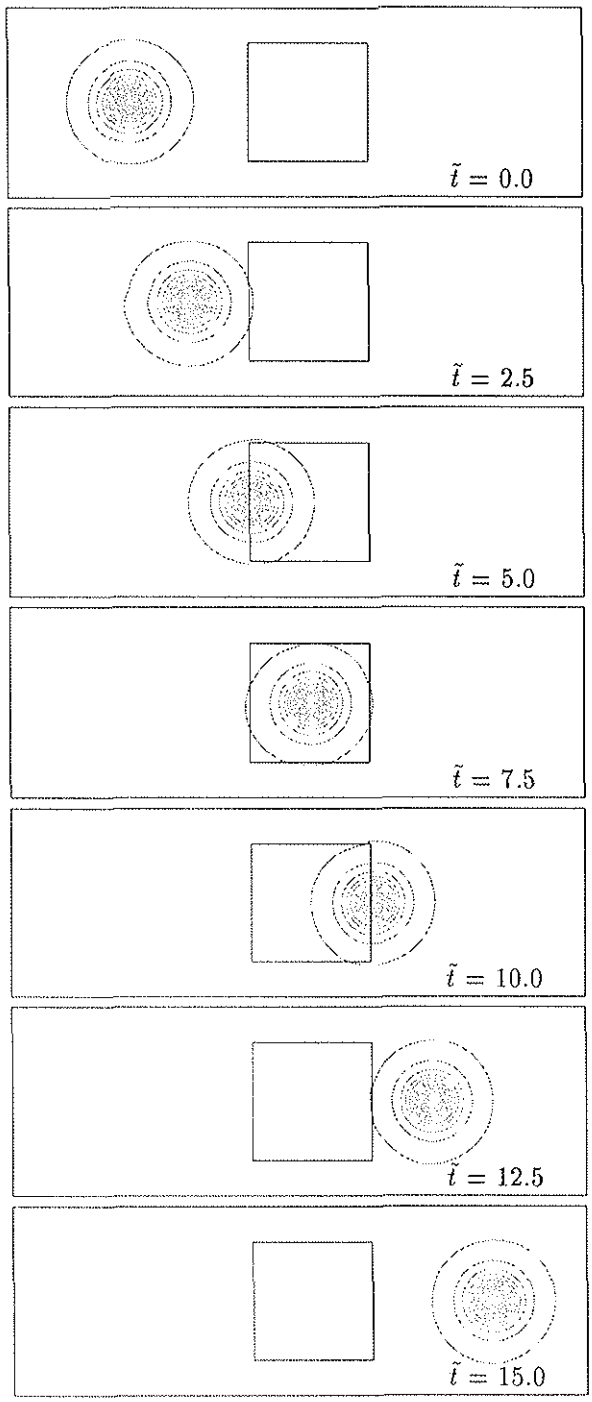

Figure 7: Convection of a vortex in to, then out of a region of local refinement.

The pressure distributions from the current computations demonstrate the ability of the code to capture the shocks sharply both above and below the aerofoil. The position and strength of the shocks are also generally in good agreement with the previous calculations.

It can also be seen that the use of local mesh refinement enables the shocks to be captured more sharply.

Convecting vortex test case

Since a particular area of interest for this problem is the convection of the incident vortex, this test case was designed to examine the behaviour of the solution as a convecting vortex crosses a mesh interface.

Figure 7 shows pressure contours of a convecting vortex as it crosses in to and then out of a refined region of the mesh. The box marked on the plots represents the outline of this refined region. The free stream Mach number of the flow, M_∞, is 0.8, the vortex strength, $\hat{\Gamma}$, is 0.2, and the refinement factor of the embedded mesh is 2.

These plots suggest that the mesh interfaces cope very well with the convecting vortex, despite the mesh discontinuity.

Interaction test case

The second case is the unsteady 2D blade vortex interaction, in which the aerofoil is considered stationary and a vortex is convected towards the blade. The conditions chosen were the interaction of a vortex of strength $\hat{\Gamma}$ = -0.2 (ie. clockwise), core radius r_c = 0.05c, with a NACA0012 aerofoil, in free stream flow of Mach number, M_∞ = 0.8, and an initial vortex-blade miss distance of y_v = -0.26c. This is the case considered numerically by Srinivasan *et al.* (Ref 8), and Damodaran & Caughey (Ref 21). The non-dimensional timescale used is defined as $\tilde{t} = U_\infty t/c$, ie. the number of chord lengths travelled by the free stream.

The computation was initialised by taking the steady flow field computed for the non-lifting aerofoil with a free stream Mach number, M_∞ = 0.8, and superimposing the flow field of the incident vortex, which is then allowed to convect towards the aerofoil. The vortex, therefore, is instantaneously imposed on the flow field at $\tilde{t} = 0$, resulting in the generation of pressure waves at the solid surfaces, as the flow adjusts to the presence of the vortex. This instantaneous imposition of a vortex is clearly an approximation of the idealised two-dimensional case (in which the vortex approaches from an infinite distance). Discrepancies between the two cases can be reduced by placing the incident vortex as far upstream as possible. This approach is clearly restricted by the computational expense of the simulation, and in the following computations the vortex has been initialised 5 chord lengths upstream of the leading edge.

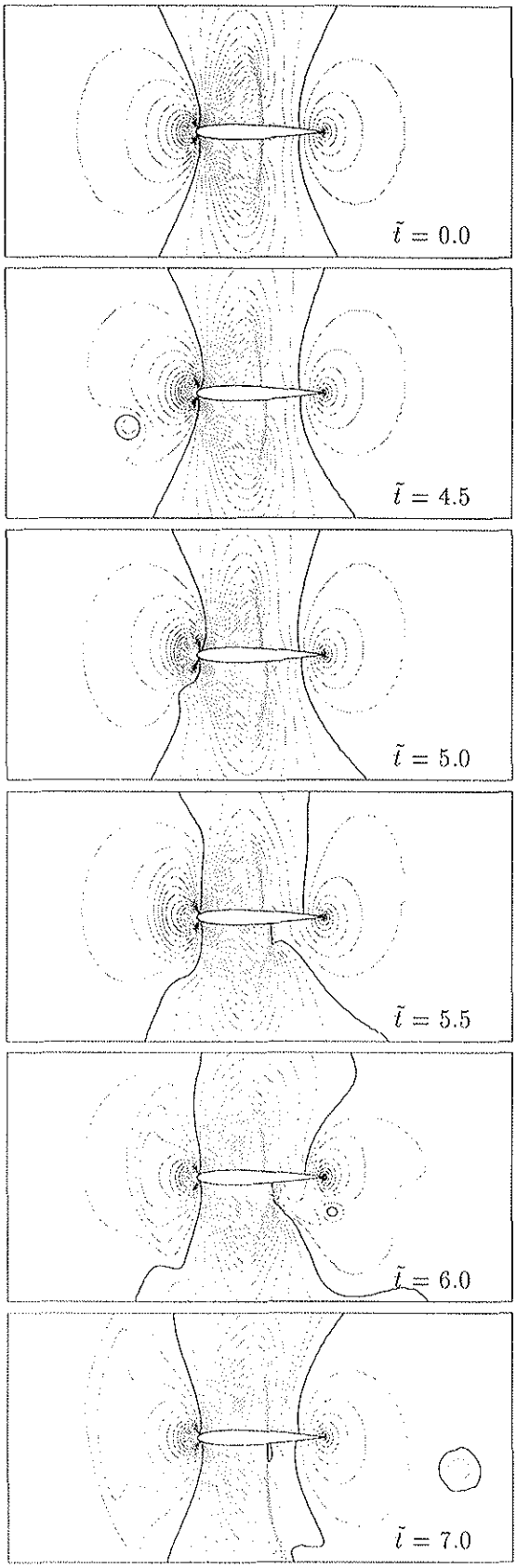

Figure 8: Pressure contours for the 2D BVI, $\hat{\Gamma}$=-0.2, r_c=0.05c, M_∞=0.8, y_v=-0.26c, NACA0012, ΔP=0.02, bold contour represents ambient pressure

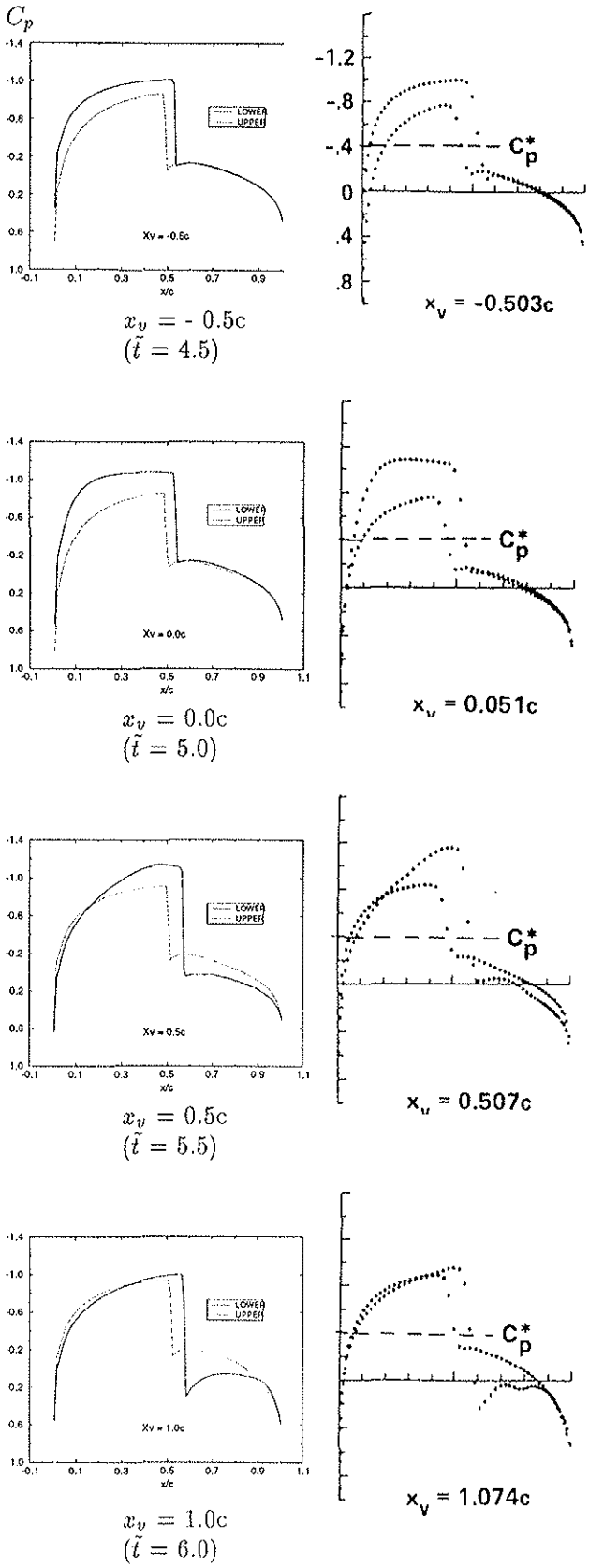

Figure 9: Surface pressure distributions (C_p against x/c) during 2D BVI. Left; current computation. Right; Damodaran & Caughey (1988)

Present computations have been made *without* the local refinement procedure and are compared to results of Damodaran & Caughey, in terms of the surface pressure distributions and the variation of the pressure fields.

The variation of the global pressure field during the interaction is shown in figure 8. These plots provide some insight into the nature of the interaction, and are in qualitative agreement with computations of Srinivasan *et al.* , and Damodaran & Caughey.

Features of the interaction which are predicted by both the current computations and also these previously published results include: the generation of an acoustic wave at the leading edge; distortion of the lower shock; and noise generation due to vortex-shock interaction.

Figure 9 shows the variation of the distributions of surface pressure coefficient during the interaction, for the current computation and also those of Damodaran & Caughey. The parameter x_v represents the position of the vortex, relative to the leading edge, normalised by the aerofoil chord length, and is directly related to the non-dimensional time $\tilde{t}$ ($x_v = \tilde{t} - 5$). A comparison of the two sets of results shows that the current computation is in good qualitative, and quantitative agreement with these previous computations.

Flow Field Analysis

To examine the noise generating mechanisms involved in the 2D BVI, the interaction is considered for a vortex of strength $\hat{\Gamma}$=-0.2 (clockwise in sense) and core size r_c=0.05c with a NACA0012 aerofoil, at zero incidence. The free stream Mach number is set to M_∞=0.8 with a vortex-blade offset of y_v=-0.10c, ie. such that the vortex trajectory passes beneath the blade. Figure 12 show the pressure field and figure 13 shows the vorticity field about the aerofoil, during the interaction.

Pressure Field

The sequence of pressure plots in figure 12 shows that there are three noise generating mechanisms,

1. Leading edge: As the vortex approaches the aerofoil, there is an induced downwash at the leading edge, causing the stagnation point to move upwards, slowing the flow along the upper surface and speeding up the flow on the lower surface. Consequently the shock on the upper surface moves upstream and weakens, whereas the shock on the lower surface moves downstream and strengthens. The vortex then moves past the leading edge and the stagnation point moves back down again. This movement of the stagnation point at the leading edge is linked with the generation of an acoustic wave which propagates upstream. This 'leading edge wave' is labelled **L** in figure 12. Figure 11 shows pressure histories at three positions upstream of the aerofoil. The position of these three stations are shown in figure 10 and are fixed relative to the blade. The pressure histories give an indication of the nature of the acoustic wave generated at the leading edge. Note that the drop in pressure at B and D are due to the movement of the pressure field associated with the incident vortex. These variations of pressure show that the acoustic wave involves an impulsive increase in pressure at all three points. At E, the pressure variation is in the form of an impulsive, positive pressure pulse. At B (directly ahead of the leading edge) this pulse is preceded by a small pressure trough, and at D this pressure trough has deepened.

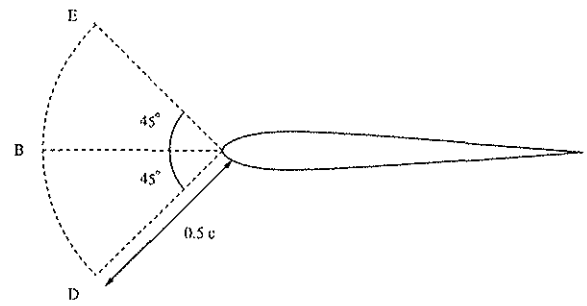

Figure 10: Points in the flow field where pressure histories are taken

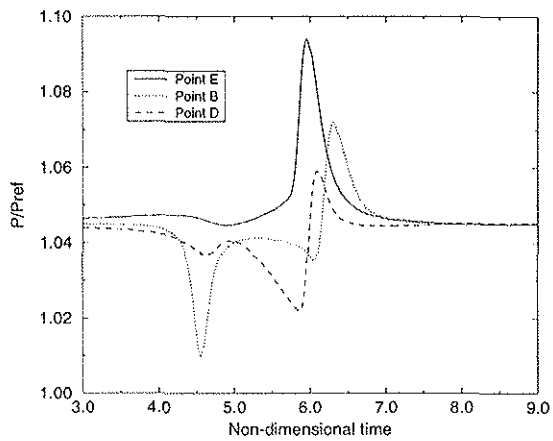

Figure 11: Pressure histories at three points in the flow-field during BVI, with a NACA0012 aerofoil. $\hat{\Gamma}$ = -0.2, r_c = 0.05c, M_∞ = 0.8, and y_v = -0.10c

2. Shock: When the vortex is convected through the shock beneath the aerofoil, there is a clear distortion of the lower shock ($\tilde{t}$ = 5.8). The interaction of the shock and incident vorticity also results in the generation of an acoustic wave which can be seen propagating down and away from the aerofoil, just downstream of the shock (figure 12, $\tilde{t}$ =6.0–6.8, labelled **S**). This acoustic wave is consistent in nature with the 'secondary wave' predicted by *Ellzey et al.* (Ref 22), or a reflected 'primary wave' predicted by Ellzey and observed by Hollingsworth & Richards (Ref 23).

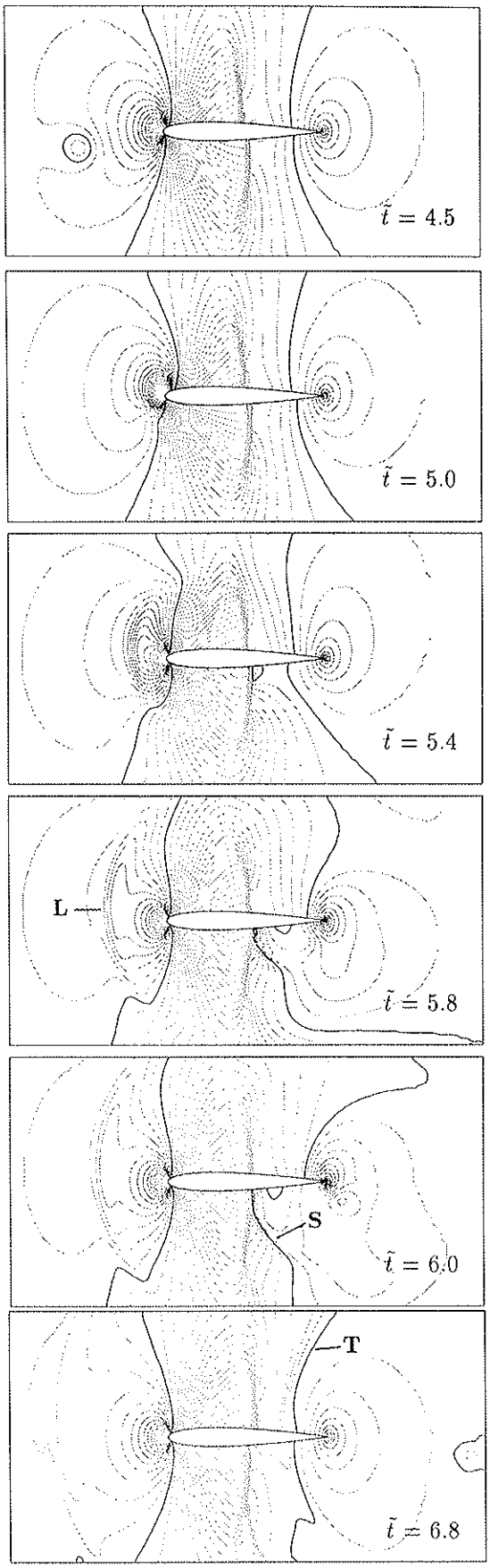

Figure 12: Pressure contours for the 2D BVI, NACA0012, $\hat{\Gamma}$ = -0.2, r_c=0.05c, M_∞=0.8, y_v=-0.10c, ΔP=0.02, bold contour represents ambient pressure

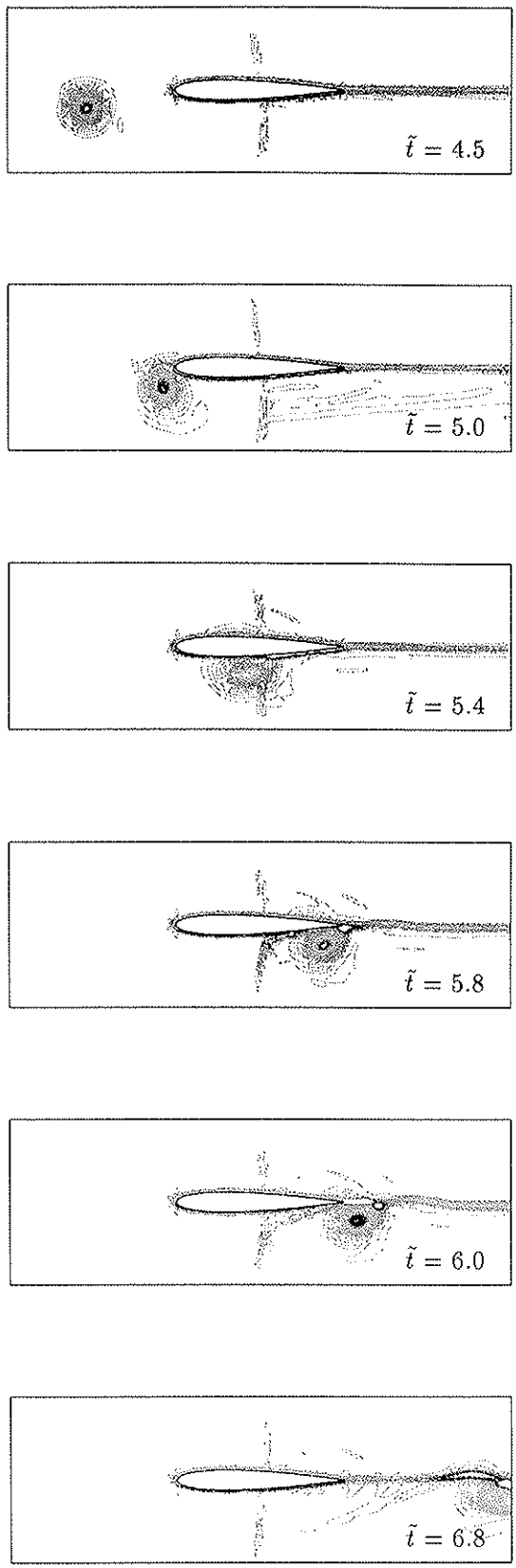

Figure 13: Vorticity contours for the 2D BVI, NACA0012, $\hat{\Gamma}$ = -0.2, r_c=0.05c, M_∞=0.8, y_v=-0.10c, $\Delta\omega$=0.02

3. Trailing edge: The passage of incident vorticity past the trailing edge appears to generate an acoustic wave which travels upstream, above the blade (figure 12, $\tilde{t}$ =6.8, labelled **T**).

Vorticity Field

The vorticity plots in figure 13 show the effect of the interaction on the incident vortex, and shocks. Even before the incident vortex has arrived at the leading edge, it is clear that vorticity has been generated around the blade and convected downstream. This vorticity is a result of numerical errors at the blade surface.

The incident vortex is split by the aerofoil leading edge and although most of the incident vorticity passes beneath the blade , a small portion can be seen moving along the upper surface. At $\tilde{t} = 5.8$, the lower shock has clearly been distorted as an effect of the vortex passing through it.

Variation in Lift

As the vortex is convected towards then past the aerofoil, there is firstly an induced downwash, then upwash on the blade resulting in a variation in lift. The lift fluctuation of the blade for this case is shown in figure 14 as a member of a family of curves. The non-smooth behaviour of the lift coefficient, when $\tilde{t}$ is less than 1, is an effect of the instantaneous flow initialisation. This plot shows the impulsive nature of the lift fluctuation, the lift reaching a minimum value as the vortex passes the leading edge of the blade. The computations have all been stopped before the lift has returned to zero.

Parameter Study

In the context of noise reduction due to BVI, aerofoil profile, $\hat{\Gamma}$ and M_∞ are very closely tied to rotor performance (and hence overall rotorcraft design) and so the most likely candidates for parameter manipulation have traditionally been y_v and r_c. For this reason these two parameters have received the most attention in attempts to study noise generation.

Effect of vortex-blade miss distance

Figure 14 shows the effect of miss distance on the lift histories of the interactions, when vortex strength and core size are fixed. This shows that the lift fluctuation becomes larger and more impulsive as the offset is decreased. The relationship between C_L, and y_v also appears to be non-linear. The nature of this relationship is more obvious in figure 15, which shows the variation of $C_{L_{min}}$ with y_v, where $C_{L_{min}}$ is the most negative value of the lift coefficient during the interaction. Again this shows that the magnitude of $C_{L_{min}}$ decreases as the offset is increased, which is due to the fall in the induced downwash velocity of the vortex with increasing radial distance. $C_{L_{min}}$ is most sensitive to variations in y_v for offsets between 2 to 5 core radii. For miss distances of less than one core radius, however, there is only a small variation of $C_{L_{min}}$ with y_v. This reduced sensitivity of $C_{L_{min}}$ to variations in y_v is due to the distributed vorticity within the core which is split by the leading edge.

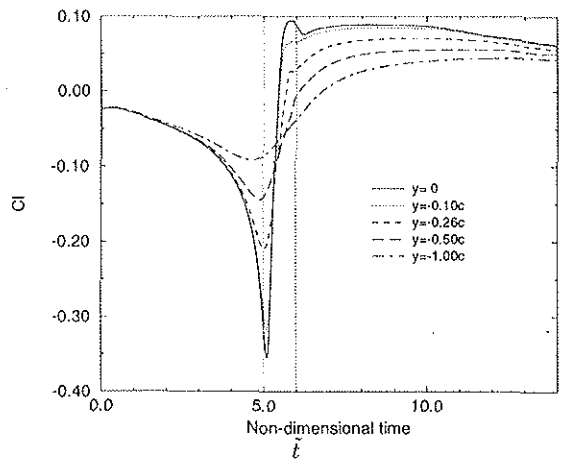

Figure 14: Effect of miss distance on lift coefficient for a NACA0012 aerofoil. $\hat{\Gamma}$ = -0.2, r_c = 0.05c, M_∞ = 0.8

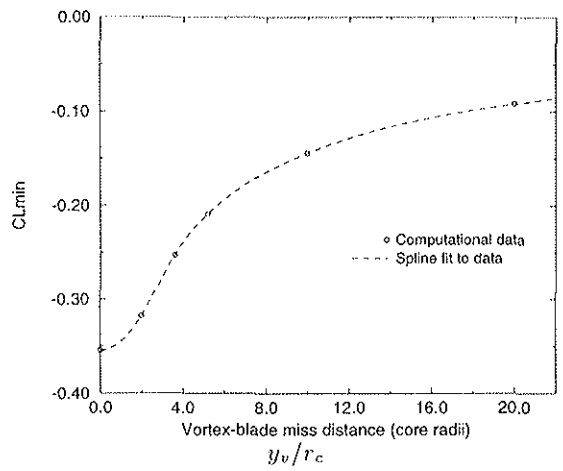

Figure 15: Effect of miss distance on Cl_{min} for a NACA0012 aerofoil. $\hat{\Gamma}$ = -0.2, r_c = 0.05c, M_∞ = 0.8

In figure 16 the effect of miss distance is described in terms of the acoustic wave generated at the leading edge. This leading edge wave is observed at the three sample points E, B and D in the flow field upstream of the blade, and defined in figure 10. It should be noted that the large drops in pressure at B and D at $\tilde{t} \approx 4.5$, are due to the pressure well associated with the incident vortex.

At E the general trend is for the pressure variation to become stronger and more impulsive as the offset is decreased. Interestingly, however, the exception, to this trend is the head-on collision for which the positive pressure perturbation is actually smaller than all the other cases presented.

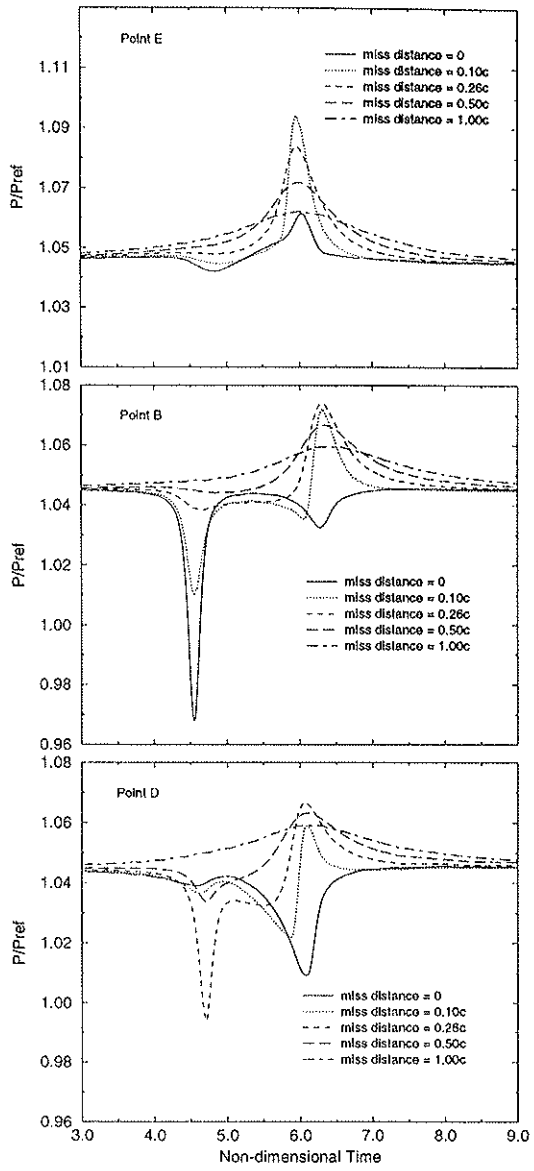

Figure 16: Effect of miss distance on noise generation for a NACA0012 aerofoil. $\hat{\Gamma}$ = -0.2, r_c = 0.05c, M_∞ = 0.8

At B (directly upstream of the leading edge) the acoustic wave is of a slightly different nature, the pressure variations showing less symmetry in time. For example at an offset of y_v = 0.10c, there is slight fall in pressure before the dominant increase. However, the trend is the same as at E – pressure variations becoming larger and more impulsive as offset is decreased. Again the head-on collision is the exception to this trend, as the pressure variation is actually negative. The magnitudes of the pressure variations at B are smaller than the corresponding variations at E.

At D the general trend is again that the pressure waves become larger and more impulsive as the offset is reduced. The head-on interaction still proves to be a special case, as there is an impulsive trough in the pressure wave as it passes through D.

This dependence of noise generation on vortex-blade offset is in agreement with the three dimensional computations of Gallman (Ref 24).

Effect of vortex core size

Figure 17 gives an indication of the effect of vortex core size on the lift fluctuations experienced by the aerofoil, for a fixed strength, Γ.

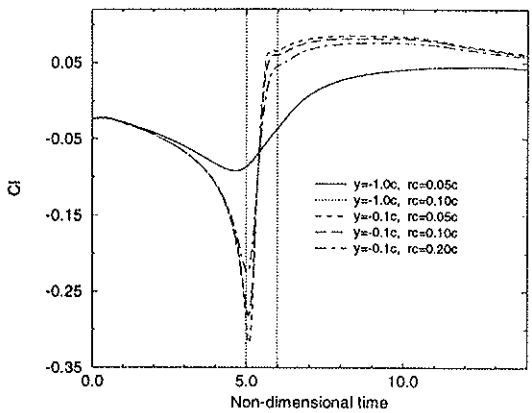

Figure 17: Effect of vortex core size on lift coefficient for a NACA0012 aerofoil. $\hat{\Gamma}$ = -0.2, M_∞ = 0.8

At an offset of y_v = 1.0c doubling the core size has no discernible effect on the lift history of the aerofoil. In figure 17, therefore, the lift history curves for core sizes of r_c = 0.05 and 0.10, at y_v = 1.0c are actually coincident. This suggests that for large miss distances the vortex core structure has little influence on the variation of lift, ie. interaction is in the 'far field' of the vortex, and the dominant parameter is the vortex strength.

For the closer interaction, however (y_v = 0.10c), the core size has a much stronger influence on the lift fluctuation. Results presented in figure 17 show that the magnitude of the lift fluctuation is reduced by increasing the core size of the incident vortex.

In terms of the numerical simulation of the interaction, it would also seem reasonable to suggest that the assumed vortex structure only significantly affects the interaction when the offset is small.

Figure 18 shows the pressure histories at three points in the flow field, E, B and D (defined in figure 10) during interactions at $\hat{\Gamma}$ = -0.2, M_∞ = 0.8, y_v = 0.1c and for varying vortex core sizes. At all three stations the acoustic waves observed are generated at the leading edge.

The top graph shows the pressure history at E. The trend is quite clear – the pressure fluctuation becomes smaller and less impulsive as the vortex core size is increased.

In the middle graph the pressure histories of point B (directly upstream of the leading edge) is pre-

sented. Note that the fluctuation at $\tilde{t} \approx 4.5$ is due to the pressure field of the incident vortex. Again the same trend can be observed – the noise generation can be significantly reduced by increasing the vortex core size.

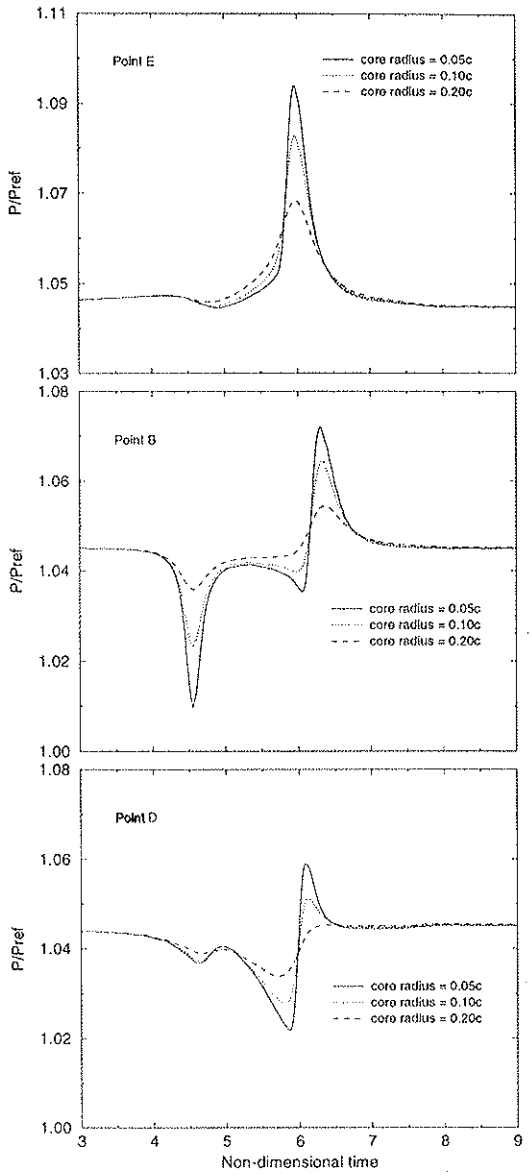

Figure 18: Effect of vortex core size on noise generation for a NACA0012 aerofoil. $\hat{\Gamma}$ = -0.2, M_∞ = 0.8

Finally, in the bottom graph the acoustic wave passing through point D can be detected, and again the magnitude of the fluctuations is clearly influenced by vortex core size.

Conclusions

The two dimensional blade-vortex interaction between a vortex of strength $\hat{\Gamma}$ = -0.2 and a NACA0012 aerofoil has been considered at a free stream Mach number of 0.8. Three noise generating mechanisms have been identified, (i) at the leading edge (ii) at the shock and (iii) at the trailing edge. The interaction has also been found to be a dependent on both the vortex-blade miss distance and the vortex core size. The leading edge acoustic wave and lift fluctuation have both been found to become larger and more impulsive as the vortex-blade miss distance is decreased. For close interactions decreasing the vortex core size also leads to stronger more impulsive noise and lift fluctuations. However, this dependence on core size was found to decrease with increasing vortex-blade miss distance.

A local mesh refinement scheme has been developed using embedded meshes and based on the method of Berger. The method allows flow/geometric features to be resolved efficiently, avoiding prohibitive computational expense.

The work presented in this paper represents the first stages of a project aimed at a comprehensive analysis of the near-field interaction, including the three dimensional case. Use of a Cartesian mesh in the far-field regions avoids the intrinsic tail-off of resolution with C or O-type grids. It is intended that this type of mesh be used in conjunction with a local refinement technique through cell subdivision, for future computations.

Acknowledgements

This project is supported by the Defence Research Agency Farnborough. The authors gratefully acknowledge this support, as well as the continued help and encouragement of Dr. Rodger Munt and Mr. Michael Spruce, DRA Farnborough.

References

[1] Berger MJ & Oliger. Adaptive Mesh Refinement for Hyperbolic Partial Differential Equations. *J. Comput. Phys.*, 53:484–512, 1984.

[2] Berger MJ & Jameson A. Automatic, Adaptive Grid Refinement for the Euler Equations *AIAA Journal* 23:561–568, 1985.

[3] Berger MJ & Colella P. Local Adaptive Mesh Refinement for Shock Hydrodynamics *J. Comput. Phys.* 82:67–84, 1989

[4] Leverton JW. 25 years of rotorcraft acroacoustics: Historical perspective and important issues. *Journal of Sound and Vibration*, 133(2):261–287, 1989.

[5] Obermeier F and Zhu KQ. Sound generation by rotor-vortex interaction in low Mach number flow. *Journal of Aircraft*, 30(1):81–87, 1993.

[6] Jones HE and Caradonna FX. Full potential modeling of blade-vortex interactions. *Vertica*,

12(1):129–145, 1988.

[7] Caradonna FX and Strawn RC. An experimental and computational study of rotor-vortex interactions. *Vertica*, 12(4):315–327, 1988.

[8] Srinivasan GR, McCroskey WJ, and Baeder JD. Aerodynamics of the two dimensional blade-vortex interaction. *AIAA Journal*, 24(10):1569–1576, 1986.

[9] Srinivasan GR and McCroskey WJ. Euler calculations of the unsteady interaction of an advancing rotor with a line vortex. *AIAA Journal*, 31(9):1659–1666, 1993.

[10] Booth ER. Experimental observations of two-dimensional blade-vortex interaction. *AIAA Journal*, 28(8):1353–1359, 1990.

[11] Kalkhoran IM & Wilson DR. Experimental investigation of the parallel vortex-airfoil interaction at transonic speeds. *AIAA Journal*, 30(8):2087–2092, 1992.

[12] Lent HM, Meier GEA, Muller KJ, Obermeier F, Schievelbusch U, and Schurmann O. Mechanisms of transonic blade-vortex interaction. *Journal of Aircraft*, 30(1):88–93, 1993.

[13] Lee S and Bershader D. Head-on parallel blade-vortex interaction. *AIAA Journal*, 32(1):16–22, 1994.

[14] Ben-Artzi M and Falcowitz J. A second-order Godunov-type scheme for compressible fluid dynamics. *Journal of Computational Physics*, 55:1–32, 1984.

[15] Hillier R. Numerical modelling of shock-wave diffraction. In *Shock waves at Marseille. Proc. 19th Int. Sym. on shock waves, vol 4* pp. 17–26, 1993.

[16] Quirk JJ. An Adaptive Grid Algorithm for Computational Shock Hydrodynamics *PhD Thesis*, Cranfield Institute of Technology, 1993.

[17] Giles MB. Nonreflecting boundary conditions for Euler equation calculations. *AIAA Journal*, 28(12):2050–2058, 1990.

[18] Tung C, Pucci SL, and Morse HA. The structure of trailing vortices generated by model rotor blades. *Vertica*, 7:33–43, 1983.

[19] Hoffman ER and Joubert PN. Turbulent line vortices. *J. Fluid Mech.*, 16(3), 1963.

[20] Van der Berg JW, Kuerten JGM, and Zandbergen PJ. Improved shock capturing of Jameson's scheme for the Euler equations. *International Journal for Numerical Methods in Fluids*, 15:649–671, 1992.

[21] Damodaran M and Caughey DA. Finite-volume calculation of inviscid transonic airfoil-vortex interaction. *AIAA Journal*, 26(11):1346–1353, 1988.

[22] Ellzey JL, Henneke R, Picone JM, and Oran ES. The interaction of a shock with a vortex: Shock distortion and the production of acoustic waves. *Phys. Fluids*, 7:172–184, 1995.

[23] Hollingsworth MA and Richards EJ. A schlieren study of the interaction between a vortex and a shock wave in a shock tube. Technical report, Aeronautical Research Council, 1955.

[24] Gallman JD. Parametric computational study of isolated blade-vortex interaction noise. *AIAA Journal*, 32(2):232–238, 1994.